Journal of Applied Geophysics 191 (2021) 104355

Contents lists available at ScienceDirect

Journal of Applied Geophysics

journal homepage: www.elsevier.com/locate/jappgeo

A geoelectrical pre-study of Älvkarleby test embankment dam: 3D forward modelling and effects of structural constraints on the 3D inversion model of zoned embankment dams

Reyhaneh Norooz [a], Per-Ivar Olsson [b,*], Torleif Dahlin [b], Thomas Günther [c], Christian Bernstone [d]

[a] School of Civil Engineering, College of Engineering, University of Tehran, Iran
[b] Engineering Geology, Lund University, Sweden
[c] Leibnitz Institute of Applied Geophysics, Germany
[d] Vattenfall AB, Sweden

ARTICLE INFO

Article history:
Received 12 October 2020
Received in revised form 25 March 2021
Accepted 27 April 2021
Available online 18 May 2021

Keywords:
Electrical resistivity tomography
Geoelectrical monitoring
Zoned embankment dam
Finite element method
Internal erosion
Structural constraints

ABSTRACT

Electrical resistivity tomography has potential as a complementary long-term monitoring method in embankment dams; however, the 3D character of the geometry including the shape of the embankment, its internal zoned construction and the reservoir water make interpretation challenging. To tackle this problem, a qualified inversion model considering the 3D environment is necessary. In this paper, prior information about the resistivity of different parts of a test embankment dam was used as constraints in order to increase the capability of defect detection in a complex 3D context. Five small defects were incorporated into the core of the model. Laboratory measurements were made on samples of the materials intended to be used for the construction of a test embankment dam, and resistivity values provided from the laboratory measurements were used in the forward modelling. A measurement sequence of around 8000 synthetic data points using extended gradient, crossline bipole-bipole and corner arrays between horizontal-horizontal, vertical-vertical, and vertical-horizontal lines were modelled and inverted all at once. The structural constraints were applied to increase the accuracy of inversion, using the L1 and L2 methods. Different mesh qualities with different boundaries for each region and 3D geometric factor calculation were applied for the inversion to evaluate the effects of region control incorporated in the inversion process. The results showed that L1 and L2 norm inversions combined with region control can determine the location of very small defects and finding the defects located near each other, respectively. Removing the region control from the inversion caused unrealistic resistivity prediction for some regions and the inability to discover the dam defects. Therefore, the proposed methodology can decrease non-uniqueness in the inversion and make time-lapse ERT a valuable monitoring tool that complements other instrumentation techniques and based on these results it was concluded promising to continue with the construction of the test dam using the same type of defects and electrode set-up, for verification under field-conditions.

1. Introduction

More than 70% of large hydropower dams are embankment dams worldwide (ICOLD, 2003). Overtopping and internal erosion are the most common reasons for embankment dam's failure (Bonelli and Nicot, 2013) while failures by slides are less common. It is essential to predict the erosion initiation at an early stage. Hence, many methods were developed to predict, calculate, or investigate leakage. The leakage water flow velocity through the core of the dam can transport soil and the detached particles are carried away gradually toward the upstream or downstream sides of the embankment or its foundation until a continuous pipe is created (Fell and Fry, 2007). Transfer of fines to the upstream side is unlikely but can for example occur in the case of reservoir level drawdowns. The weak zones affected by the erosion in the impermeable core has, compared to the surrounding soil, high electrical resistivity values, and these defects are detectable by Electrical Resistivity Tomography (ERT).

Many embankment dams have been designed and built many years ago when the dam safety aspects of design criteria such as seismic considerations and geotechnical engineering were less advanced compared to modern standards. For example, the general understanding has been improved on aging processes that can lead to internal erosion which ultimately can threaten the stability of such dams. From the equipment perspective, recent advances in instrumentation techniques provide more frequent and comprehensive data than in the past. For example, ERT has been tested as a new continuous monitoring method in

* Corresponding author at: Engineering Geology LTH, Lund University, Box 118, SE-22100 Lund, Sweden.
E-mail address: per-ivar.olsson@tg.lth.se (P.-I. Olsson).

https://doi.org/10.1016/j.jappgeo.2021.104355
0926-9851/

embankment dams (Sjödahl et al., 2008; Sjödahl et al., 2009). Some studies also used ERT to discover the defects and soil water content in the embankment dam bodies, dikes and the abutments (Ikard et al., 2015; Masi et al., 2020). Quality control during dam construction is another issue that can be checked using ERT measurements and quality of soil compaction can be investigated using ERT data (Lin et al., 2018). Furthermore, the method can be used for site investigation of the foundation before constructing the dam to detect possible problematic zones from a stability or hydraulic point of view (Batayneh et al., 2001; Niederleithinger et al., 2015). ERT measurements provide significant distributed information about the interior of the dam in comparison to the discrete piecewise information that piezometers, pressure cells, inclinometers, horizontal movement gauges and temperature sensors provide. In particular, time-lapse ERT measurements can provide valuable data over time and indicate resistivity changes in different parts of the dam, which can provide some hints about internal problems. These methods are time and cost-effective and are, when applied to zoned embankment dams, capable of finding existing resistivity contrasts due to different moisture content, temperature changes and varying porosity (Johansson and Dahlin, 1996). From the hydropower asset perspective, the possibility to utilize these technology advancements is quite limited since sensor cables cannot without great difficulties and with considerable safety concerns be placed in the materials close to the impermeable core of existing embankment dams. Even sampling of the materials can be challenging (Ekström et al., 2019). Before optimal placement of sensor cables could even be considered, there is a need to demonstrate what can be achieved in pilot-scale blind-test experiments. Synthetic modelling of geophysical methods suitable for the monitoring of embankment dam performance is useful tools in this context, where the results can provide guidance on how to set up such pilot-scale experiments. This paper presents the results from such a pre-study in respect of ERT. In 2D ERT the inversion approach assumes a 2D subsurface model and neglects the resistivity changes perpendicular to the profile. In 2D surveys carried out along zoned embankment dam the results suffer from severe 3D effects caused by these zones, slopes and reservoir should be considered (Sjödahl et al., 2006). Some researchers used 2D measurements with 3D geometric factors in order to mitigate the 3D effects in the 2D data to some extent (Bièvre et al., 2018). Hennig et al. (2005) used different configurations combined with the topography correction method to modify geophysical effects. Cho et al. (2014) investigated 3D effects on 2D resistivity measurements in earth dams and concluded that water level changes in the reservoir affect the 2D resistivity data and may distort the models. They used an independent reference model of time-lapse and original reference data to overcome 3D effects. Cho and Yeom (2007) assessed crossline tomography for detecting anomalous seepage paths in an embankment dam. They used 3D finite element forward modelling and 2.5D inversion. Their results yielded reasonable information about the weak zones, but the interpretation was challenging. Fargier et al. (2014) used a 3D extended normalization approach to remove the 3D effects from 2D data.

The purpose of this study is to assess the capability of ERT measurements with different arrays as a monitoring approach for internal defect detection of embankment dams, and the capability of structural constraints for increasing the accuracy of ERT models. With this purpose, a 3D model of a test embankment dam containing some defects in the core with the height of 4 m in Älvkarleby was made and around 8000 3D synthetic data were generated using the pyGIMLi package (Rücker et al., 2017). The horizontal measurement profiles were placed along the clay till core from the left to the right abutment at different heights and vertical profiles were placed at the end of the core near the abutments and different arrays were used for the data collection. The data sets were inverted using the pyBERT/pyGIMLi package (Rücker et al., 2017). In this research, 3D geometry calculation combined with structural constraints was used to assess 3D inversion results. A reference-model-based strategy with a full minimization was also applied while the model without defects was considered as the reference.

2. The Älvkarleby test dam and laboratory measurements

The hydropower operator Vattenfall has for the reasons outlined above built a pilot-scale embankment dam in Älvkarleby in order to assess the damage detection capability of several dam monitoring methods, including electrical resistivity tomography (ERT). The dam was built as a conventional zoned embankment dam, in a concrete container with the inner dimension of 20 m * 16 m * 4 m (Fig. 1). The reinforcement of the bottom slab consists of high resistive glass fibre (rather than low resistive steel bars), thereby resembling a hard rock foundation. The scale of the dam is large enough to illustrate challenges to be met by real-case situations, while still small enough to be manageable in a controlled test rig. Resistivity values obtained through laboratory measurements of the materials intended for construction were used in the 3D forward modelling, on samples provided by Vattenfall and their local aggregate supplier. In addition, measurements were made on the reservoir water from the test site provided by Vattenfall.

Cylindrical Plexiglas sample holders with an inner diameter of 53.8 mm were used for the laboratory measurements. Current was sent through the samples via stainless steel plate electrodes at each end of the sample, and potential measurements were made using gold plated pins inserted through holes in the plastic cylinder at 50 mm separation. An ABEM Terrameter LS2 was used for the measurements that were repeated 6 times for each material sample, using 1, 5 and 10 mA transmitted current, and an average of the measured data used. For the water sample, 4 repetitions were used.

The material samples were prepared by packing the provided wetted sample material into the sample holders to simulate saturated conditions. The provided water from the site was used for the wetting. Measurements were also taken with a water-filled cylinder to assess the water resistivity. Measurements were made on core and fine filter material, whereas the coarse filter sample was too coarse-grained (8–64 mm) to fit in the sample container.

The room temperature was 24 °C in the laboratory in which the material had been stored and was tested. Temperature corrections relative to 18 °C (Ward, 1990) were applied to the measured results which are used for the presented resistivities. The averaged resistivities are summarized in Table 1. The low resistivity of the core material is indicative of high clay content.

3. Finite element forward modelling

To simulate the zoned embankment dam (Fig. 2), pyGIMLi, which is an open-source package for modelling and inversion was used (Rücker et al., 2017). The software package uses the finite element method, which is suitable from a modelling perspective, for the complex embankment dam geometry and 3D configurations at hand. The geoelectrical modelling is governed by the following differential equation:

$$-\nabla[\sigma(x,y,z)U(x,y,z)] + \nabla j_s(x,y,z) = 0 \quad (1)$$

in which σ is the electrical conductivity, U is the electrical potential and J_s is the current density. The Neumann boundary condition is applied in all surfaces, assuming that atmospheric boundaries are infinitely resistive. The fibre glass reinforced concrete foundations as well the steel bar reinforced right, and left abutments are assumed to be infinitely resistive as well. This poses a simplification of model geometry and boundaries to simplify modelling which would however only be correct if they were coated with an electrically insulating layer during the construction.

The M and N potential values are the numerical solution of Eq. 2 and the apparent resistivity can be calculated as follows:

Fig. 1. Aerial view of Älvkarleby test dam.

Table 1
Resistivity of water and material samples from laboratory measurements.

Material	Resistivity at 18 °C [Ωm]
Water	243
Type A: Core	21
Type B: Fine filter	185

$$\rho_a = KR = K\frac{\Delta V_{MN}}{I} \tag{2}$$

where ρ_a is the apparent resistivity, K is the geometric factor and ΔV_{MN} is the electrical potential difference between electrodes M and N. Apparent resistivity is the synthetic ERT data, which needs to be inverted using suitable inversion techniques.

The modelled dam has 20 m perpendicular length and 4 m height (Fig. 3a). The water level in the reservoir was considered constant at the height of 3 m in the simulations. In the actual test dam, the water body extends only to the upstream toe of the embankment. However, with the upstream toe still being relatively far away from the investigated core, the difference in size of the water body is not expected to have a significant impact on the modelling results. The material resistivity values used in the modelling, which are presented in Table 2 are based on the laboratory measurements in combination with literature references (Sjödahl et al., 2006; Sjödahl et al., 2008; Schön, 1996; Schopper, 1982).

Five targeted defects, which resemble small-scale realistic damages in the impermeable core of an embankment dam, were arbitrarily placed at different positions in the core (see Fig. 3 b and Table 3). The defect number 1 can be thought of as a cavity in the dam, for example due to an empty wooden box accidently built into a dam while the defects numbered 2 to 5 can be thought of as from internal erosion and fines leaving the dam. Defect number 1 is modelled by introducing a void in the model geometry (Neuman boundary condition) while the other defects are modelled through a contrasting resistivity.

The concrete container that the embankment rests on was assumed to have infinitely high resistivity. In case the concrete is coated with an electrical insulation layer this will be correct; otherwise, some current will flow in the concrete, how much will depend on the resistivity of the concrete which will vary depending on curing state and moisture content. In this case, the current would also flow in the ground surrounding the concrete container, to which extent would depend on the resistivity of the ground and the concrete. In order to model the influence of possible current flow in the concrete, the FE-model would have to be expanded to include the container as well as the surrounding ground (a river sand deposit). However, this was not carried out in this study.

In order to calculate the geometric factor, an embankment dam with constant conductivity of 1 S/m (a homogenous model space) was assumed. Thus, the 3D effects due to the outer geometry are considered, and it is possible to obtain the true geometric factor. To check the 3D calculation of geometric factor, the resistivity of 100 Ωm was assumed in all parts of the dam. The 3D forward modelling using pyGIMLi was performed and the apparent resistivity values were calculated. The average,

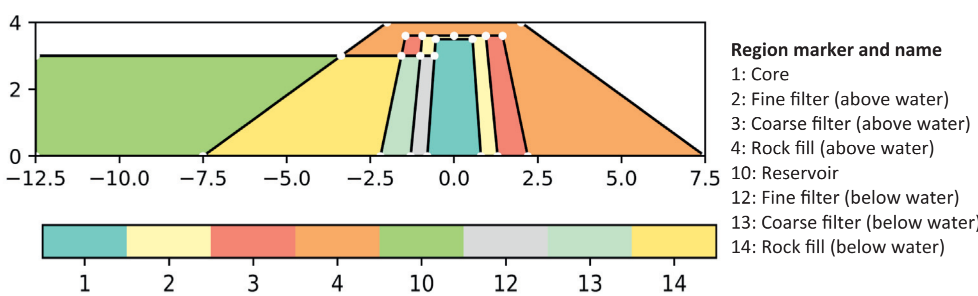

Fig. 2. Cross-section of the FE modelled dam with region markers and their name.

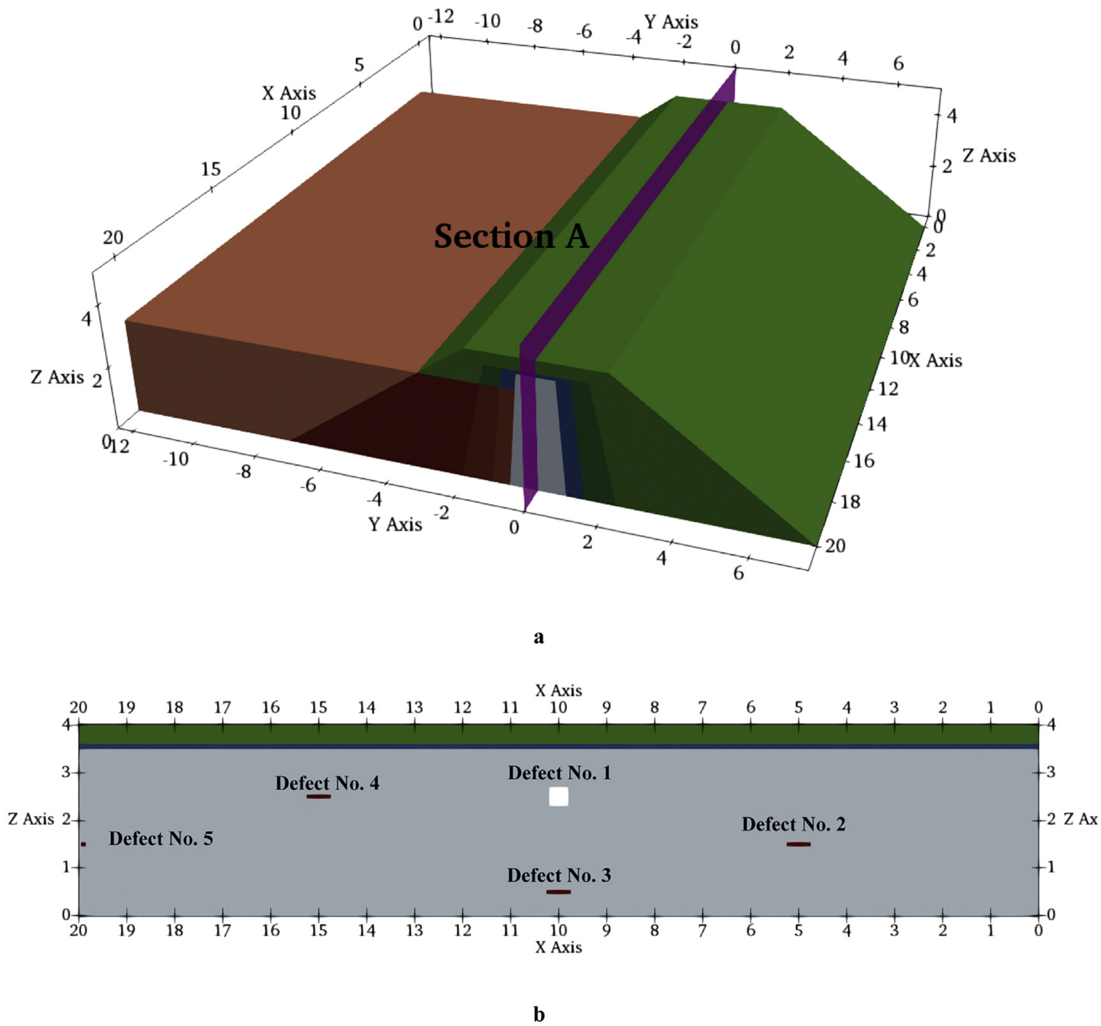

Fig. 3. Position of defects in the core; a) Position of cross-section planes of A; b) Section A and the position of defects in the core.

Table 2
Material resistivity used in the forward modelling.

Region	Resistivity (Ωm)	Material marker
Reservoir	240	10
Core	21	1
Fine filter (above water)	1000	2
Coarse filter (above water)	2000	3
Fine filter (below water)	180	12
Coarse filter (below water)	500	13
Rock fill (above water)	20,000	4
Rock fill (below water)	1500	14

minimum and maximum values of the calculated apparent resistivity considering all 8000 data points are around 101.05, 99.88 and 101.16 Ωm, respectively. The differences between the real (100 Ωm) and calculated resistivity values are 0.2 and 1.160% for minimum and maximum values, respectively.

Fig. 4 shows the 3D placement of modelled ERT survey lines together with the dam geometry. Six horizontal buried electrode lines with 63 cm electrode spacing were modelled: on top of the clay core (red) and at two levels in the filters adjacent to the core, bottom (brown) and middle (pink). In addition, four vertical electrode lines were modelled with 50 cm vertical spacing at each end in the filter of the dam (yellow and blue).

Different types of configurations were used in the finite element forward modelling. Crossline bipole-bipole array, similar to the cross-hole

Table 3
Simulated defects placed in the clay core. Defect No. 1 was a hole in the clay core.

Defect No.	Shape	Size			Coordinate of the centre point	Resistivity (Ωm)
		Δx	Δy	Δz		
1	Cube	0.4 m	0.4 m	0.4 m	(10,0,2.5)	Void
2	Cuboid	0.5 m	1.3 m	0.1 m	(5,0,1.5)	180
3	Cuboid	0.5 m	1.4 m	0.1 m	(10,0,0.5)	180
4	Cuboid	0.5 m	1.2 m	0.1 m	(15,0,2.5)	180
5	Cuboid	0.1 m	1.3 m	0.1 m	(19.9,0,1.5)	180

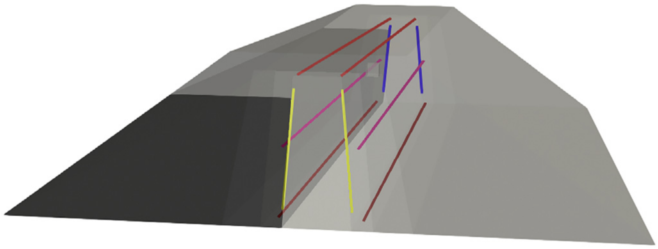

Fig. 4. Position of measurement lines.

bipole-bipole array (Zhou and Greenhalgh, 2000), was used between the six horizontal lines at different depth with eleven different combinations, which contains 3681 data points (see Table 4). In this array, the current is injected into two opposite electrodes in two parallel lines and the potential is measured between four pairs of electrodes on either side of the current electrodes in two parallel lines. Measurements were taken for n-factors 1–4 with perpendicular AM-BN electrode combinations, plus three with the nearest diagonal for the potential electrodes in both directions. Bipole-bipole array was also used between the inclined end lines (see Table 4).

Extended gradient array (Zhou et al., 2020) was applied in each six horizontal lines and 3636 data points were collected totally (see Table 4). This array is an extension of the well-proved multiple gradient array which provides data with good signal-to-noise ratio and valuable information content in a time-efficient way in real application (Dahlin and Zhou, 2006).

A corner shaped array (Tejero-Andrade et al., 2015) was placed at each end, including one horizontal line in the bottom and one inclined line. Current electrodes were fixed in each line and the potential electrode pairs were moved toward the corner and in the next step the position of current electrodes was changed, and the same process was repeated (see Table 4).

A corner array at each end of the dam was applied containing one horizontal line in the bottom or top and one inclined line in the end (see Table 4) and 224 data points were calculated. The current electrodes were set at the end of each line and the potential electrodes placed in the same way in one side of the current electrodes and shifted toward the corner. Afterwards, the current electrodes were shifted one step toward the corner and the potential electrodes shifted accordingly. The corner arrays are suitable for finding deep anomalies (Tejero-Andrade et al., 2015).

The measurement profiles were designed in a way to provide sufficient data points which can cover the whole core volume and increase the defect detection capability while at the same time adhere to the layered construction procedure of the dam. To improve core data coverage, the profiles were placed in the direct vicinity of the core and not for example in a regular grid-shaped pattern which would cause reduction of coverage in some areas of the core. The Crossline measurements between horizontal profiles at different elevations could cover the middle area of the core. The Crossline measurements between the inclined profiles near the right and left abutments obtained enough data points to discover probable defects near the abutments. The corner arrays between the inclined and horizontal lines could cover the areas near the upstream and downstream borders of the core and the fine filter. Furthermore, extended gradient array applied in each horizontal line supported other collected data points in addition to obtaining data near the upstream and downstream core borders with the filter.

Table 4
Combinations used in the finite element forward modelling.

Array type	Combination name	Number of data points
Bipole-bipole	Cross lines in the same levels with 3 combinations	1227
Bipole-bipole	Cross lines in the different levels with 8 combinations	2454
Extended gradient	In the 6 horizontal lines	3636
Multiple gradient	Between end line and the bottom lines with 4 combinations	252
Corner	Between end line and the bottom or top lines with 8 combinations	224
Bipole-bipole	Between inclined lines at the ends with 4 combinations	148
Total collected data points		7941

4. Synthetic modelling

For assessing the forward modelling accuracy, three different mesh qualities were generated with different number of cells: approximately 700′000, 2′000′000 and 5′000′000. A tetrahedral mesh with refined mesh elements around critical points was used for the modelling. The differences between the three mesh types were evaluated to make sure that the mesh quality and the synthetic data are reliable. Quadratic shape functions were used for data generation with fine and medium meshes. Apparent resistivity relative change percentage between different mesh sizes was calculated as follows:

$$\text{apparent resistivity relative change} = \frac{\rho^a_{fine} - \rho^a_{coarse}}{\rho^a_{fine}} \quad (3)$$

where ρ^a_{coarse} and ρ^a_{fine} are the apparent resistivity calculated applying coarse mesh and fine mesh, respectively. The maximum, median and mean values of the apparent resistivity relative difference between different mesh sizes are shown in Table 5. The maximum relative changes between the coarse-medium mesh and medium-fine mesh are around 16.76 and 7.93%, respectively. However, the average changes between medium-fine mesh are as low as 0.3% and thus the medium mesh on average gives similar modelling results as the fine mesh. Fig. 5 shows the apparent resistivity relative difference between coarse-medium mesh and medium-fine mesh. The relative difference between medium-fine mesh is very small and can be neglected.

A comparison of the geometric factors between different mesh sizes was made. The 3D geometric factor in the coarse-medium mesh and medium- fine mesh has changed up to 10.41 and 0.18%, respectively, which indicates that using a finer mesh is not justifiable and a medium-mesh size is sufficient. The medium mesh size with the quality of q = 1.2 used in the modelling is shown in Fig. 6. The mesh quality values (q values) are radius-edge ratio (Si, 2015), which determines the desired tetrahedron quality, where higher values lead to worse mesh quality and thus numerical accuracy (Miller et al., 1995).

5. Inversion

The Boundless Electrical Resistivity Tomography (BERT) software package (Günther et al., 2006) was used for the inversion. Several tetrahedral mesh sizes were generated by the software TetGen (Si, 2015)

Table 5
Apparent resistivity relative difference between different mesh sizes in percentage.

	Apparent resistivity relative change between the coarse-medium mesh (%)	Apparent resistivity relative change between the medium-fine mesh (%)
Maximum	16.76	7.93
Median	0.98	0.10
Mean	1.30	0.30

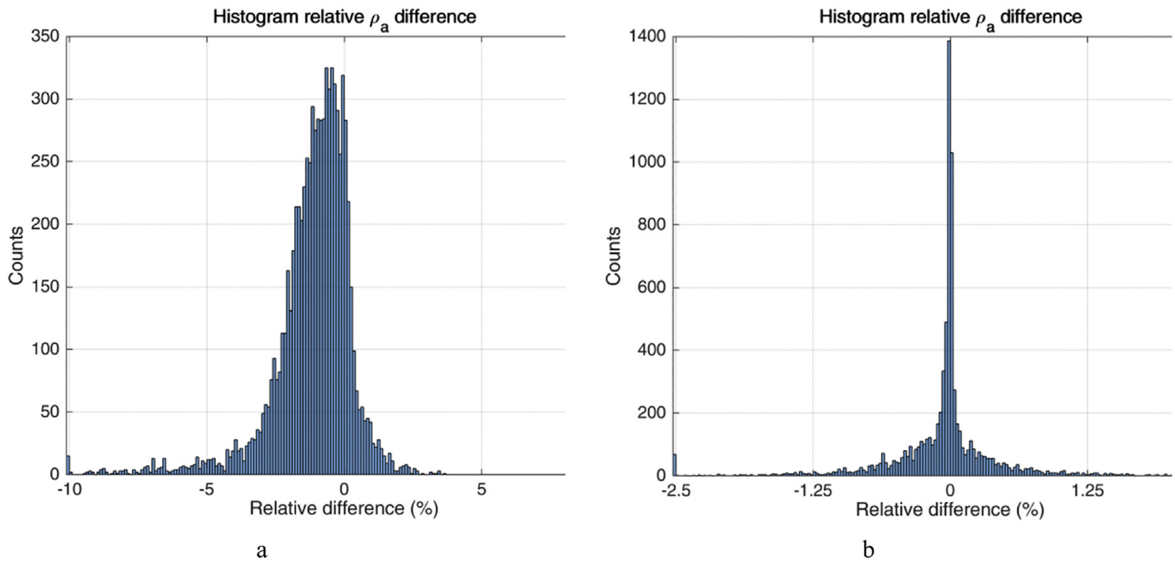

Fig. 5. a) Apparent resistivity relative difference between coarse and medium meshes in percentage. b) Apparent resistivity relative difference between fine mesh and medium mesh in percentage.

with q values between 1.19 and 1.6 associated with 600′000 to 120′000 cells, respectively. The number of cells in the inversion calculations which is controlled by the q values as well as the local refinement were less than the forward modelling calculations to reduce calculation time to a practical range. However, for q less than 1.19, shortage of memory error did not allow to refine the mesh any further. The results of q = 1.2 which contain approximately 550′000 cells were much better than q = 1.4 or larger while they did not have differences with the results of q = 1.19 and thus the 1.2 quality value was applied for the meshing in this paper.

For all models, to avoid smooth transitions, robust (L1) methods were applied in addition to the L2-norm of the model roughness. Optimization of regularization strength was used in such a way that the data were fit within error bounds ($\chi^2 = 1$ means a perfect match). The Jacobian matrix was recalculated in each iteration. Because of the layered construction approach used when building embankment dams (the compaction of materials is layer by layer and these separate layers have an impact on the measured resistivities), an anisotropic regularization (Coscia et al., 2011) factor of 0.06 and a Lambda value of 200 were used. First-order smoothness constraints were applied in each dam region, whereas the constraints are disconnected at known material boundaries (for example between core and fine filter, between fine filter and coarse filter, between coarse filter and support fill, etc.). Noise was assumed to be 1% plus a voltage resolution of 1 mV. Resistivity ratio values considering the model without defects as the reference were calculated for some models. In this strategy, a minimization is applied in each frame while the model is constrained to the first and next frames. The inversion results for L1 norm and L2 norm inverted with the mesh quality of 1.2 and without any prior information, except for decoupling structural constraints between the different zones (regions), are shown in Fig. 7 and Fig. 8, respectively. As can be seen, these models are not capable of predicting the correct resistivity values of the different regions. The L2 norm inversion predicted the resistivity values of different parts slightly better than the L1 norm inversion. It estimated that the resistivity values of water reservoir and clay core as the conductive parts and dam toe as the resistive part are correct while the L1 norm inversion erroneously depicted the water reservoir as being the most resistive part. None of these models could predict the position of the defects clearly. The L1 norm inversion indicated continuous resistive zones in the bottom and top of the core (Fig. 7 b) which were not correct while it showed the defect No. 5 position properly. The L2 norm inversion predicted a resistive region on the top of the core, which was not factual

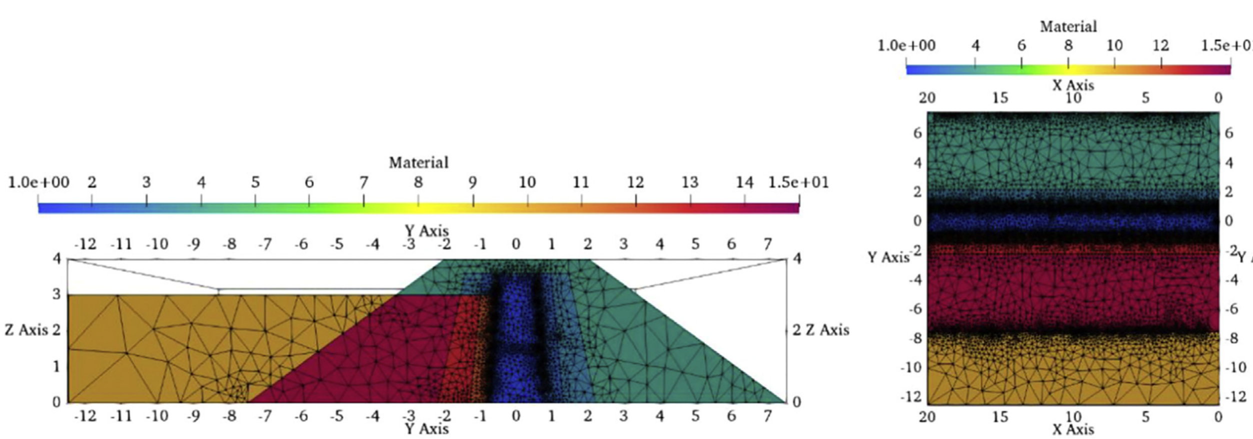

Fig. 6. Medium mesh with around 2′000′000 cells, quality of 1.2 and quadratic shape function used in the forward modelling.

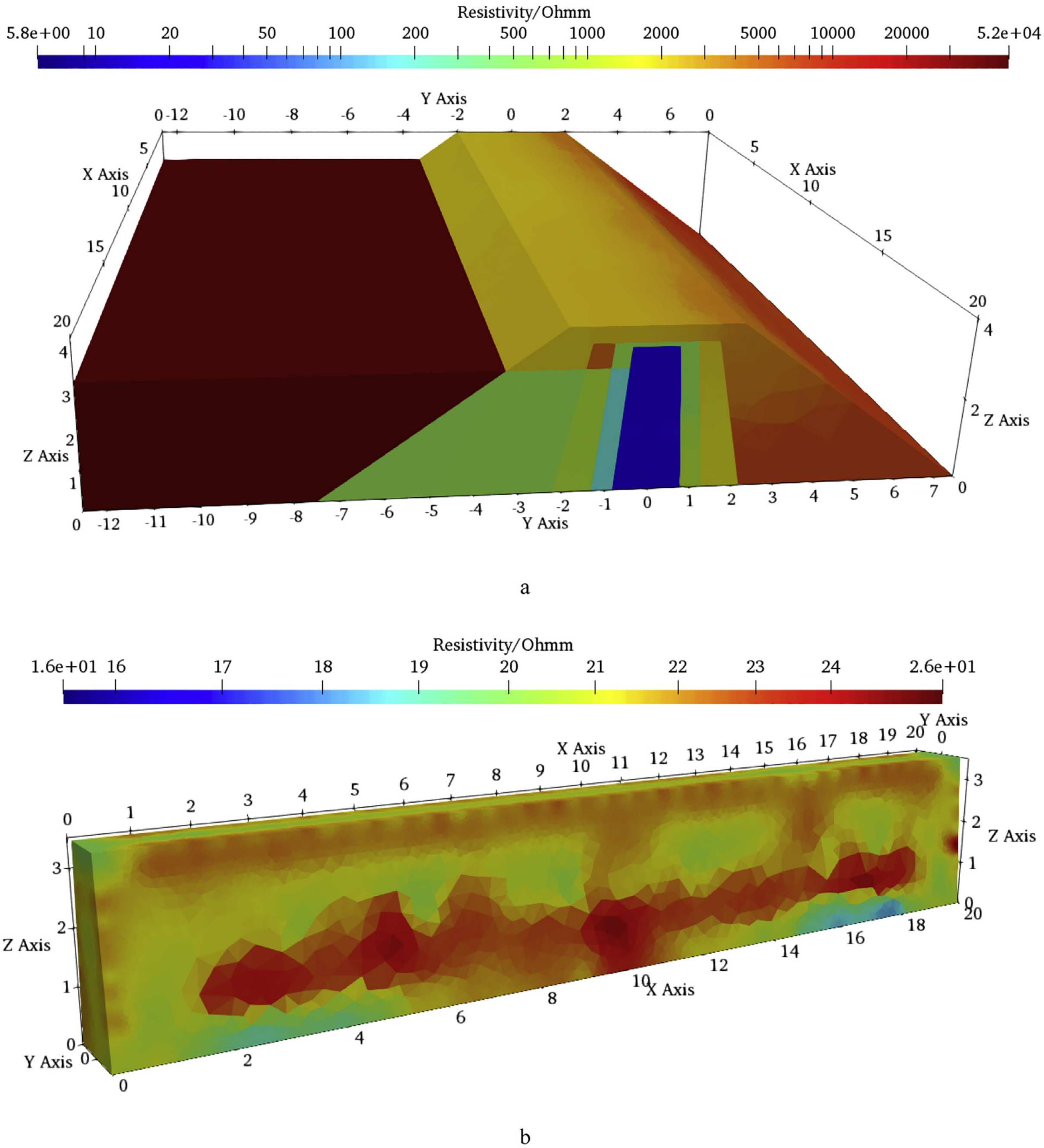

Fig. 7. L1 norm Inversion results for model containing 5 defects in the clay core without region control. a) L1 norm inversion results of whole model. b) Inversion results of the core in L1 norm model.

(Fig. 8 b). Although it appropriately foresees the defect positions in some ways, the interpretation was still challenging because of the existence of many false anomalies.

In the next step, prior information concerning the known distribution of materials in the embankment were applied in the inversion, that is the core, the filters, and the support fill, with and without water saturation, plus the water reservoir. Different region control files (settings for the constraints inside of the individual regions) with various boundaries were applied in the inversion to evaluate effects of the different boundary intervals (Table 6 and Table 7). In Table 6 narrower boundaries were used. In the first region control, the starting model with the real resistivity values was chosen. The lower and upper bounds for the filter, rock fill and water regions were 20% lower and higher than the starting model values, respectively. For the core, the upper boundary was increased up to 200 Ωm.

In the second region control, the starting model, lower and upper bounds of the filter, rock fill and water region were the same as first region control. But the starting model and upper bound of the core region were changed to 60 Ωm and 200 Ωm, respectively.

In the third region control, the starting model, lower and upper bounds of the filter, rock fill and water region were the same as the first and second region control. The upper boundary of the core was increased up to 2000 Ωm. The starting model of the core was chosen the same as the first region control.

Finally, a fourth region control was run using the normal boundaries for each region with 20% interval around the real resistivity values and

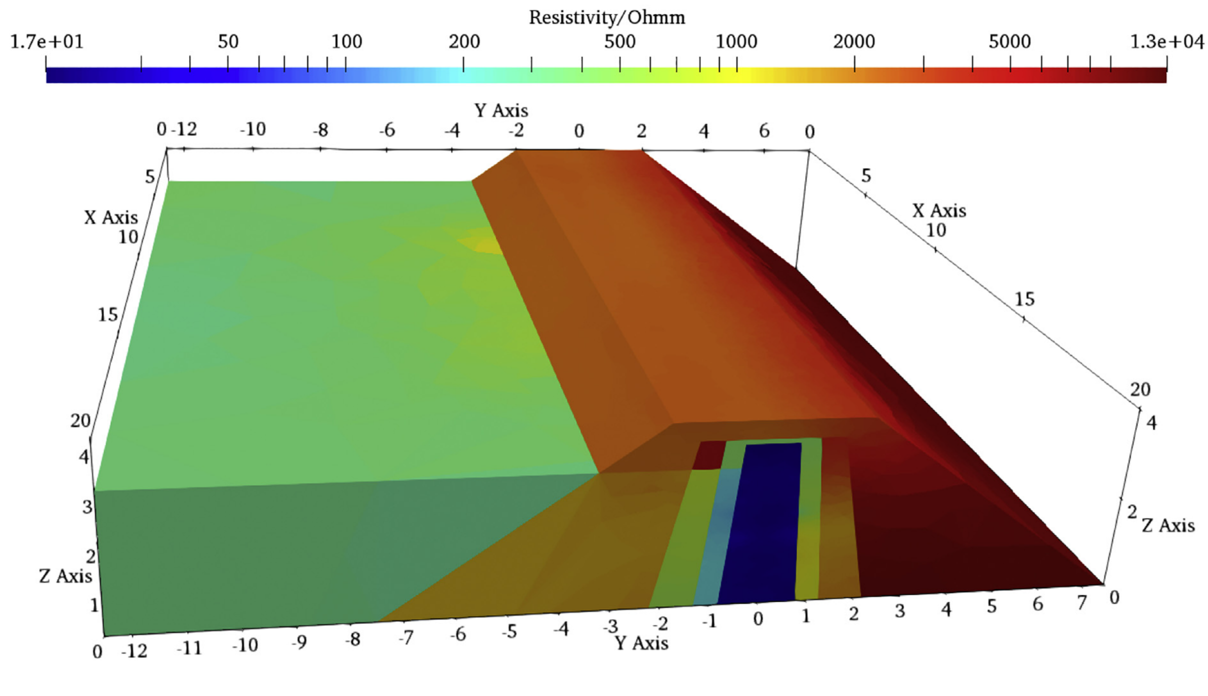

a

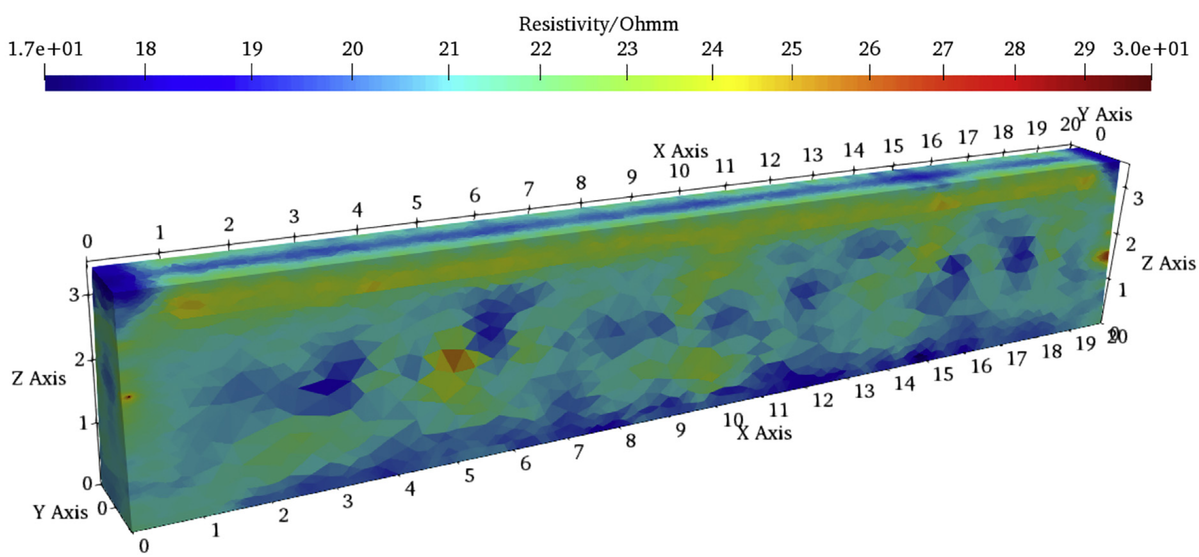

b

Fig. 8. L2 norm Inversion results for model containing 5 defects in the clay core without region control. a) L2 norm inversion results of whole model. b) Inversion results of the core in L2 norm model.

Table 6
Start value, lower and upper bounds for the region controls with broad boundaries used in the inversions (R1 to R4). Note that only the results for region control 3 are shown in the paper.

Material marker	Region	Start value				Lower bounds				Upper bounds			
		R1	R2	R3	R4	R1	R2	R3	R4	R1	R2	R3	R4
1	Core	21	60	21	21	12.6				200	200	20,000	29
2	Fine filter (above water)	1000				600				1400			
3	Coarse filter (above water)	2000				1200				2800			
12	Fine filter (below water)	180				108				252			
13	Coarse filter (below water)	500				300				700			
4	Rock fill (above water)	20,000				12,000				28,000			
14	Rock fill (below water)	1500				1500				2100			
10	Water	240				144				336			

Table 7
Start value, lower and upper bounds for the region controls with narrow boundaries used in the inversions (R1 to R4). Note that only the results for region control 3 are shown in the paper.

Material marker	Region	Start value				Lower bounds				Upper bounds			
		R1	R2	R3	R4	R1	R2	R3	R4	R1	R2	R3	R4
1	Core	21	60	21	21	16.8				200	200	20,000	25.2
2	Fine filter (above water)	1000				800				1200			
3	Coarse filter (above water)	2000				1600				2400			
12	Fine filter (below water)	180				144				216			
13	Coarse filter (below water)	500				400				600			
4	Rock fill (above water)	20,000				16,000				24,000			
14	Rock fill (below water)	1500				1200				1800			
10	Water	240				192				288			

the starting model for each region was chosen to be the same as the real resistivity values. The broader boundaries that were used are specified in Table 7. Here, the same strategy as for the narrower boundaries was used for the broader boundaries, with around 40% interval for filter, rock fill and water regions instead of 20%.

In the following, the inversion results of the models containing the prior information are presented. The inversion results in the clay core were extracted from the model to investigate the defect positions. The results are shown from both sides of the core as explained in Fig. 9 (view 1 and 2). In addition, four cross-sections in the defect location in the core were taken out to assess the capability of the models in predicting the defect locations (Fig. 9).

The inversion results of the clay core for region control 3 with narrow and broad boundaries and mesh quality of q = 1.2 are shown in Fig. 10. The maximum and minimum inverted resistivity values in both models are approximately the same (Fig. 10 a and b). In the model with narrower boundaries, the defect locations are more visible. The results of both models show that the current models are unable to identify the exact position of defects if they are located close to each other. It should be noted that Defect No. 5, which has the smallest volume, is detectable by using this new approach in the inversion.

In the first region control, the upper boundary of the clay core was limited to 200 Ωm. The results of this model are similar to the model with third region control and decreasing the upper boundary has no effect on finding the defect locations and resistivity values. The resistivity ratio values for blocky models with the third region control and a mesh quality of q = 1.2 are shown in Fig. 10 c and d. The regions with larger resistivity ratio values are the location of defects. The model with larger boundaries could show the location of defects close to each other precisely while it also produces some false anomalies.

For some calculations, different values between q = 1.19 and q = 1.6 were used to inspect the effects on the inversion results. The inversion results of the blocky models with the third region control and with of q = 1.19 and q = 1.4 are shown in Fig. 11 a and b, respectively. The inversion results with q = 1.19 are similar to q = 1.2, while q = 1.4 results could not find the location of the defects in Section 3 and found lots of false anomalies.

The L2 model norm inversion was used with different region controls and different boundaries and with the same mesh quality q = 1.2 in order to compare the results with the L1 norm (blocky model option) inversion (Fig. 12). All the L2 inversion results show some anomalous parts in addition to the real defects. Compared to the L1 norm inversion results, it can be added that the L2 norm inversion performs better in separating the position of the defects close to each other. Fig. 12 c and d show the resistivity ratio values for the L2 norm models with the third option. The models with broader boundaries show frequent false anomalies.

Inversion parameters, calculation time and memory usage for each model are summarized in Table 8. The models without boundaries needed more iterations and longer calculation time, while the results

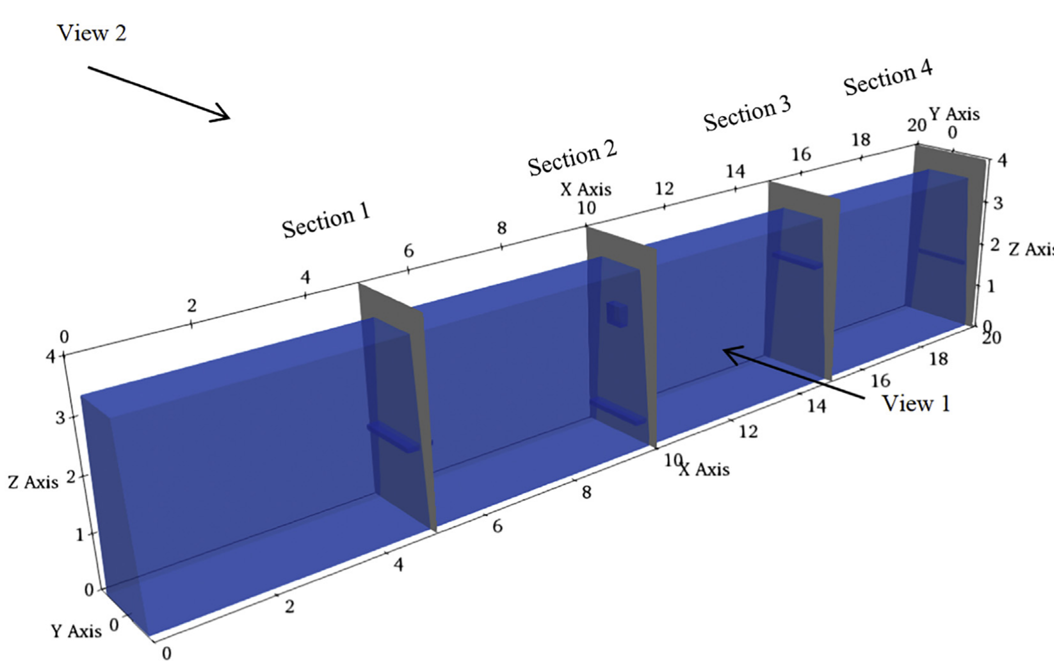

Fig. 9. The cross-sections used in the defect locations.

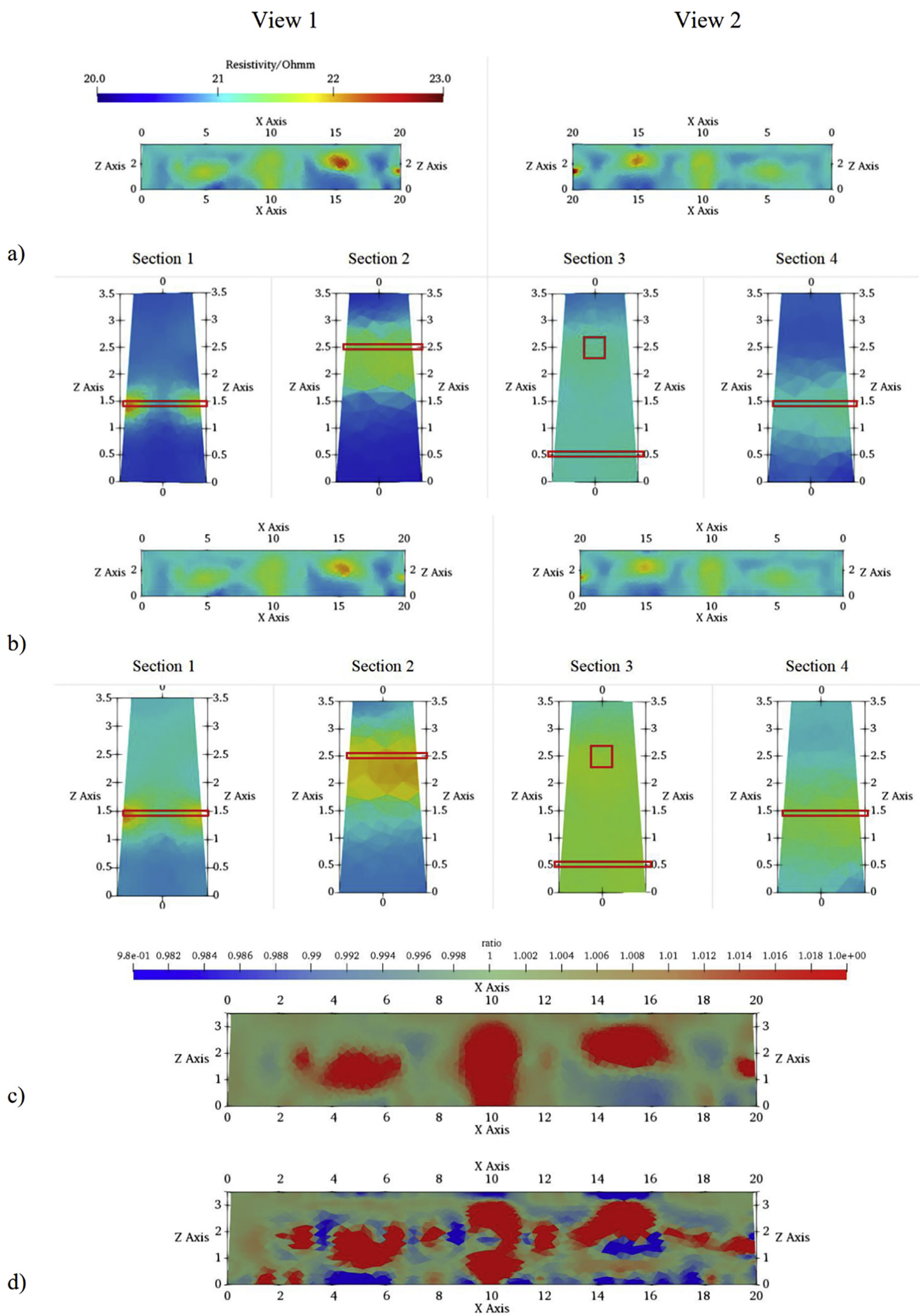

Fig. 10. The inversion results of the clay core for model containing 5 defects in the clay core with region control 3. a) Blocky model option with Narrow boundaries. b) Blocky model option with Broad boundaries. c) Resistivity ratio of blocky models with Narrow boundaries. d) Resistivity ratio of blocky models with Broad boundaries.

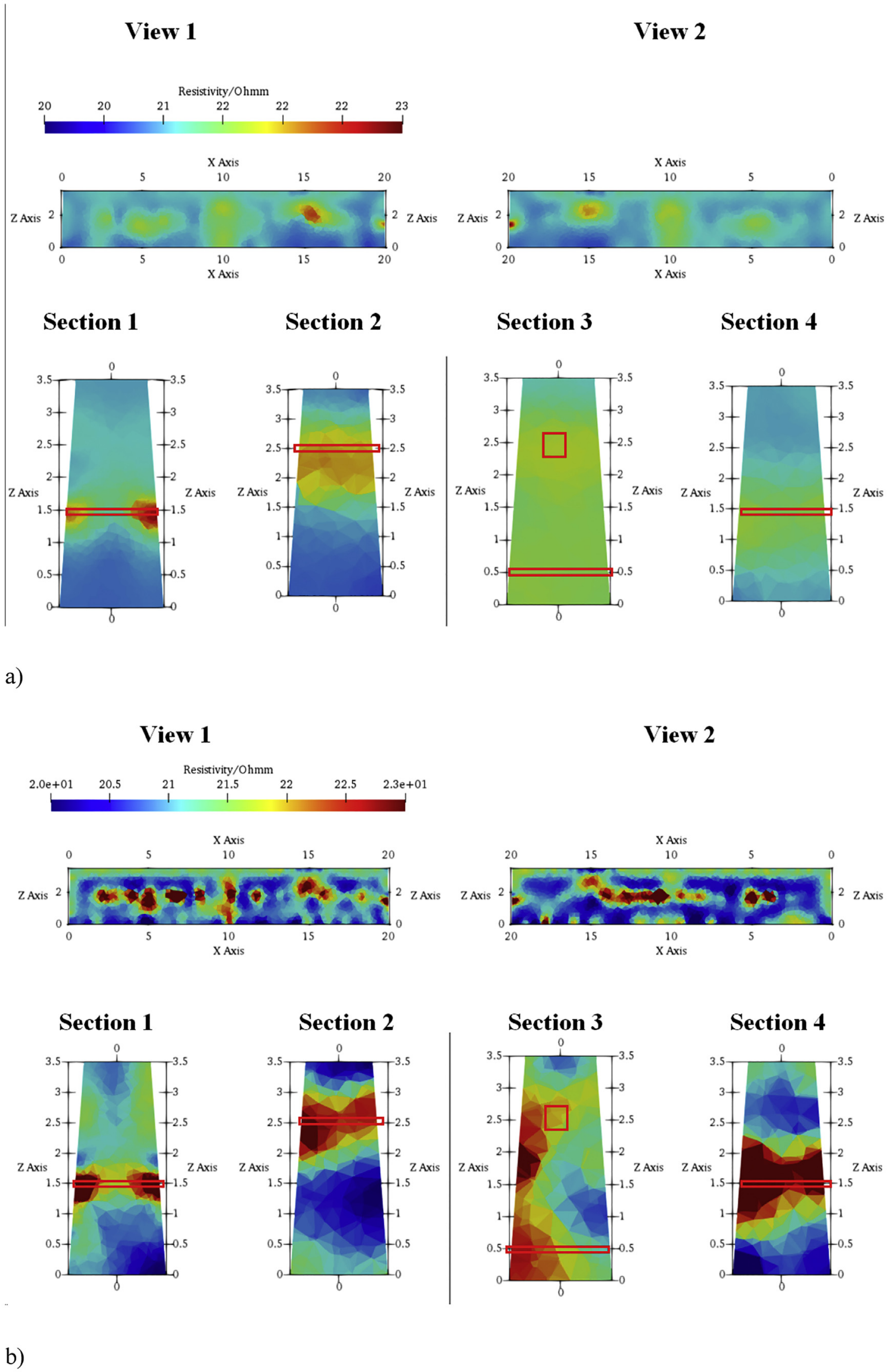

Fig. 11. The inversion results of the clay core for model containing 5 defects in the clay core with region control 3. a) Blocky model option with Narrow boundaries with the mesh quality of 1.19. b) Blocky model option with Narrow boundaries with the mesh quality of 1.4.

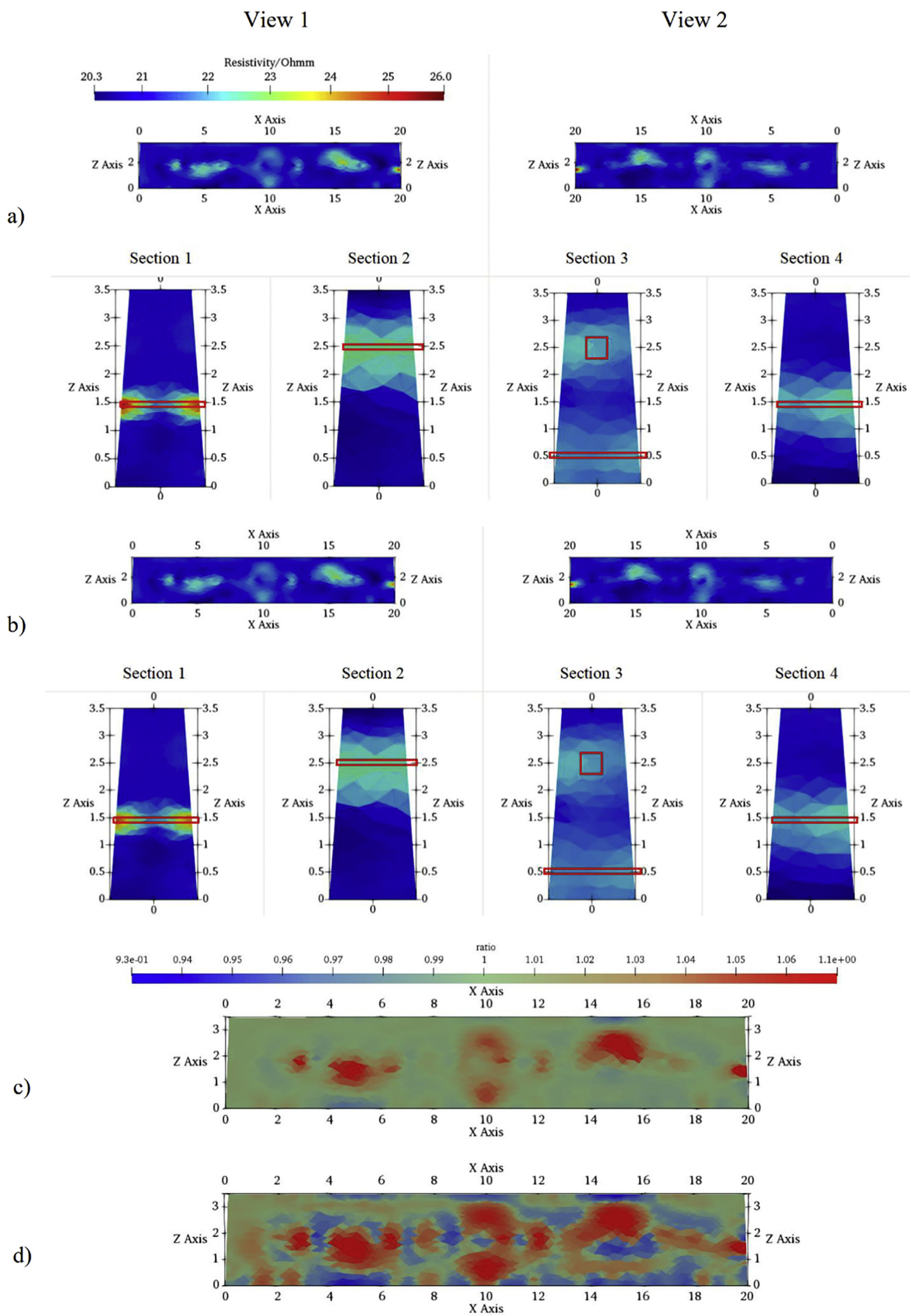

Fig. 12. The inversion results of the clay core for model containing 5 defects in the clay core with region control 3. a) L2 norm model option with Narrow boundaries. b) L2 norm model option with Broad boundaries. c) Resistivity ratio of L2 norm models with Narrow boundaries. d) Resistivity ratio of L2 norm models with Broad boundaries.

Table 8
Inversion parameters of the synthetic dataset. RRMS: relative root mean square error.

Model	Iterations	Chi2	RRMS	Memory usage (gigabytes)	Calculation time (hours)
NarrowBoundary-L1-region control 1	3	1.10	0.011	49.8	19.5
NarrowBoundary-L1-region control 2	4	1.04	0.010	49.9	27.7
NarrowBoundary-L1-region control 3	3	1.09	0.011	49.8	19.6
NarrowBoundary-L1-region control 4	3	0.98	0.010	49.8	22.6
NarrowBoundary-L2-region control 1	3	1.09	0.011	49.8	13.2
NarrowBoundary-L2-region control 2	3	1.09	0.011	49.8	23.2
NarrowBoundary-L2-region control 3	3	1.08	0.010	49.8	13.2
NarrowBoundary-L2-region control 4	3	1.01	0.010	49.8	39.9
BroadBoundary-L1-region control 1	3	0.94	0.010	49.9	68.4
BroadBoundary-L1-region control 2	3	0.95	0.010	49.8	70.2
BroadBoundary-L1-region control 3	3	0.93	0.010	49.9	69.0
BroadBoundary-L1-region control 4	3	0.93	0.010	49.9	45.1
BroadBoundary-L2-region control 1	3	0.98	0.010	49.9	36.1
BroadBoundary-L2-region control 2	3	0.99	0.010	49.9	42.8
BroadBoundary-L2-region control 3	3	0.97	0.010	49.9	36.6
BroadBoundary-L2-region control 4	3	0.90	0.010	49.8	36.7
L1-withoutboundary	6	0.46	0.013	49.9	128.9
L2-withoutboindary	9	0.17	0.009	49.9	104.6

were not satisfying in predicting the defects' location. The calculations of the models with the structural constraints were time-effective and furthermore more precise in finding the defects' locations.

6. Conclusions

ERT monitoring, based on strategically placed sensor cables in embankment dams, is a promising tool for detecting realistic small-scale damages in the core of embankment dams. However, the complex 3D nature of the dam geometry and the small size of the defects complicate the task. To tackle the problem, the outer geometry (topography) and the internal zones of the dam (for example, filters) must be integrated in 3D inversion. Calculation of the 3D geometric factor was used as part of the interpretation process, based on finite element forward modelling that considers the 3D real geometry of the dam and constant conductivity of 1 S/m for all regions.

Forward modelling using the pyGIMLi software package was performed on a 3D model of the embankment dam including the reservoir water, and 8000 synthetic data points were collected. The synthetic data were inverted in 3D using the BERT package, decoupling the smoothness constraints between the different zones (core and filters) of the embankment dam. L1 and L2 norm inversion was tested with different internal region control combinations.

Inversion with decoupling of the structural constraints along known internal material boundaries, but without prior knowledge of the resistivity values of the different regions, showed that the models were neither able to estimate the correct resistivities nor the defect locations inside the test dam.

Better results were achieved with the known resistivity values of different dam regions used as prior information. Different resistivity bounds for each segment of the dam were tested, including narrow and broad intervals. Furthermore, a time-lapse inversion scheme considering the prior information was performed based on the model without defects as the reference model. The results show that:

1. Decoupling of the smoothness constraints along known material borders is necessary but not sufficient, as it can produce erroneous resistivity distributions and fail to locate the defects.
2. A-priori data on expected resistivity ranges for the internal zones in the embankment dam gives inversion models that can detect the defects. With broader boundaries some anomalous zones were produced, while narrower ranges give more accurate predictions.
3. L1 model norm (blocky) inversion can detect the correct position of the defects but cannot discriminate zones that are located close to each other.
4. L2 model norm inversion is capable of finding the defects located near each other while it produces some false anomalies.
5. Time-lapse inversion based on the above findings can predict the location of the defects well.

Based on the results of a pre-study of the research presented in this paper, plus similar studies for other techniques, Vattenfall designed several defects (at for researchers' unknown position), built into a pilot-scale embankment dam at their laboratory facilities in Älvkarleby. The experiment to assess the capability of different dam monitoring methods, including electrical resistivity tomography (ERT) in finding defect positions, is in progress. The electrode spreads for the ERT monitoring surround the clay core and around 8000 data points are measured daily using a similar sequence as the one tested here.

Declaration of Competing Interest

The authors declare that they have no known competing financial interests or personal relationships that could have appeared to influence the work reported in this paper.

Acknowledgement

The authors wish to express our gratitude to Energimyndigheten (project 48411-1) and Vattenfall AB for funding this project. Matteo Rossi and Nikolas Höglund did set up the initial model of the embankment dam in BERT/GIMLi and made the simulations on it, which we used as a base for the work presented here, which is gratefully acknowledged. The computations were performed on resources provided by the Swedish National Infrastructure for Computing (SNIC) at LUNARC. We wish to thank our colleagues at LUNARC for valuable support in connection with the study.

References

Batayneh, A.T., Abdallah, S.A.Z., Abdelruhman, A.A., 2001. Geophysical investigations for the location of a proposed dam in Al Bishriyya (Al Aritayn) area, northeast Badia of Jordan. Environ. Geol. 40, 918–922.

Bièvre, G., Oxarango, L., Günther, T., Goutaland, D., Massardi, M., 2018. Improvement of 2D ERT measurements conducted along a small earth-filled dyke using 3D topographic data and 3D computation of geometric factors. J. Appl. Geophys. 153, 100–112.

Bonelli, S., Nicot, F., 2013. Erosion in Geomechanics Applied to Dams and Levees. John Wiley & Sons, Inc., Hoboken. USA.

Cho, I.-K., Yeom, J.-Y., 2007. Crossline resistivity tomography for the delineation of anomalous seepage pathways in an embankment dam. Geophysics 72, 31–38.

Cho, I.-K., Ha, I.-S., Kim, K.-S., Ahn, H.-Y., Lee, S., Kang, H.-J., 2014. 3D effects on 2D resistivity monitoring in earth-fill dams. Near Surface Geophys. 12, 73–81.

Coscia, I., Greenhalgh, S., Linde, N., Doetsch, J.A., Marescot, L., Günther, T., Vogt, T., Green, A., 2011. 3D crosshole ERT for aquifer characterization and monitoring of infiltrating river water. Geophysics 76, 49–59.
Dahlin, T., Zhou, B., 2006. Gradient array measurements for multichannel 2D resistivity imaging. Near Surface Geophys. 4, 113–123.
Ekström, I., Ljunggren, M., Viklander, P., 2019. Large-scale sonic drilling to determine supporting fill parameters. Association of State Dam Safety Officials Annual Conference. Orlando, Florida, 15 September 2019.
Fargier, Y., Palma, Lopes S., Fauchard, C., Francois, D., Côte, P., 2014. DC-electrical resistivity imaging for embankment dike investigation: a 3D extended normalization approach. J. Appl. Geophys. 103, 245–256.
Fell, R., Fry, J.J., 2007. Internal Erosion of Dams and their Foundations. CRC Press, London 9780429083051, p. 245.
Günther, T., Rücker, C., Spitzer, K., 2006. Three-dimensional modelling and inversion of dc resistivity data incorporating topography– II. Inversion. Geophys. J. Int. 166, 506–517.
Hennig, T., Weller, A., Canh, T., 2005. The effect of dike geometry on different resistivity configurations. J. Appl. Geophys. 57, 278–292.
Ikard, S.J., Rittgers, J., Revil, A., Mooney, M.A., 2015. Geophysical investigation of seepage beneath an earthen dam. Groundwater. 53 (2), 238–250.
International Commission On Large Dams (ICOLD), 2003. World Register of Dams. http://www.icold-cigb.org.
Johansson, S., Dahlin, T., 1996. Seepage monitoring in an earth embankment dam by repeated resistivity measurements. Eur. J. Environ. Eng. Geophys. 1, 229–247.
Lin, C.-H., Lin, C.-P., Hung, Y.-C., Chung, C.-C., Wub, P.-L., Liu, H.-C., 2018. Application of geophysical methods in a dam project: Life cycle perspective and Taiwan experience. J. Appl. Geophys. 158, 82–92.
Masi, M., Ferdos, F., Losito, G., Solari, L., 2020. Monitoring of internal erosion processes by time-lapse electrical resistivity tomography. J. Hydrol. 589.
Miller, G.L., Talmor, D., Teng, S.-H., Walkington, N., Wang, H., 1995. A Delaunay based numerical method for three dimensions: generation, formulation, and partition. Proceeding of 27th Annual ACM Symposium on the Theory of Computing, pp. 683–692.
Niederleithinger, E., Abraham, O., Mooney, M., 2015. Geophysical methods in Civil Engineering: overview and new concept. International Symposium Non-Destructive Testing in Civil Engineering (NDT-CE) September 15–17. Berlin. Germany.
Rücker, C., Günther, T., Wagner, F.M., 2017. pyGIMLi: an open-source library for modelling and inversion in geophysics. Comput. Geosci. 109, 106–123.
Schön, J., 1996. Physical properties of rocks: fundamentals and principles of petrophysics. Handbook of geophysical exploration. Vol. 18. Redwood Books. Trowbridge.
Schopper, J.R., 1982. Electrical conductivity of rocks containing electrolytes. Landolt-Börnstein, Group V, Vol 16. Physical Properties of Rocks. Springer, pp. 276–291.
Si, H., 2015. TetGen, a Delaunay-Based Quality Tetrahedral Mesh Generator: ACM Transactions on Mathematical Software (TOMS), 41. https://doi.org/10.1145/2629697.
Sjödahl, P., Dahlin, T., Zhou, B., 2006. 2.5D Resistivity modeling of embankment dams to assess influence from geometry and material properties. Geophysics 71, 107–114.
Sjödahl, P., Dahlin, T., Johansson, S., Loke, M.H., 2008. Resistivity monitoring for leakage and internal erosion detection at Hällby embankment dam. J. Appl. Geophys. 65, 155–164.
Sjödahl, P., Dahlin, T., Johansson, S., 2009. Embankment dam seepage evaluation from resistivity monitoring data. Near Surface. Geophysics. 7, 463–474.
Tejero-Andrade, A., Cifuentes, G., Chávez, R.E., López-González, A.E., Delgado-Solórzano, C., 2015. L- and CORNER-arrays for 3D electric resistivity tomography: an alternative for geophysical surveys in urban zones. Near Surface Geophys. 13, 355–367.
Ward, S.H., 1990. Resistivity and Induced Polarization Methods, Geotechnical and Environmental Geophysics. Society of Exploration Geophysicists, Tulsa, pp. 147–189.
Zhou, Bing, Bouzidi, Youcef, Ullah, Saif, Asim, Muhammad, 2020. A full-range gradient survey for 2D electrical resistivity tomography. Near Surface Geophysics 18 (6), 609–626. https://doi.org/10.1002/nsg.12125.
Zhou, B., Greenhalgh, A.A., 2000. Cross-hole resistivity tomography using different electrode configurations. Geophys. Prospect. 48, 887–912.